IJMMM International Journal of Minerals, Metallurgy and Materials 矿物冶金与材料学报（英文版）

Study on the ion behavior of solid-phase reaction synthesis of iron chromite at 1473 K

Yan Wang, Peiyuan Ni, Yuling Liu, and Tengfei Deng

Cite this article as:
Yan Wang, Peiyuan Ni, Yuling Liu, and Tengfei Deng, Study on the ion behavior of solid-phase reaction synthesis of iron chromite at 1473 K, *Int. J. Miner. Metall. Mater.*, (2025). https://doi.org/10.1007/s12613-024-3007-4

View the article online at SpringerLink or IJMMM Webpage.

Articles you may be interested in

Saida Shaik, Zhiyuan Chen, Preeti Prakash Sahoo, and Chenna Rao Borra, Kinetics of solid-state reduction of chromite overburden, *Int. J. Miner. Metall. Mater.*, 30(2023), No. 12, pp. 2347-2355. https://doi.org/10.1007/s12613-023-2681-y

Jing Wen, Hongyan Sun, Tao Jiang, Bojian Chen, Fangfang Li, and Mengxia Liu, Comparison of the interface reaction behaviors of $CaO–V_2O_5$ and $MnO_2–V_2O_5$ solid-state systems based on the diffusion couple method, *Int. J. Miner. Metall. Mater.*, 30(2023), No. 5, pp. 834-843. https://doi.org/10.1007/s12613-022-2564-7

Junyi Xiang, Xi Lu, Luwei Bai, Hongru Rao, Sheng Liu, Qingyun Huang, Shengqin Zhang, Guishang Pei, and Xuewei Lü, Oxidation behavior of FeV_2O_4 and $FeCr_2O_4$ particles in the air: Nonisothermal kinetic and reaction mechanism, *Int. J. Miner. Metall. Mater.*, 31(2024), No. 8, pp. 1839-1848. https://doi.org/10.1007/s12613-024-2851-6

Yufeng Guo, Jinlai Zhang, Shuai Wang, Jianjun Fan, Haokun Li, Feng Chen, Kuo Liu, and Lingzhi Yang, Diffusion and reaction mechanism of limestone and quartz in fluxed iron ore pellet roasting process, *Int. J. Miner. Metall. Mater.*, 31(2024), No. 3, pp. 485-497. https://doi.org/10.1007/s12613-023-2739-x

Zihang Yan, Qing Zhao, Chengzhi Han, Xiaohui Mei, Chengjun Liu, and Maofa Jiang, Effects of iron oxide on crystallization behavior and spatial distribution of spinel in stainless steel slag, *Int. J. Miner. Metall. Mater.*, 31(2024), No. 2, pp. 292-300. https://doi.org/10.1007/s12613-023-2713-7

Xudong Mao, Pritesh Garg, Xiaojun Hu, Yuan Li, Samik Nag, Saurabh Kundu, and Jianliang Zhang, Kinetic analysis of iron ore powder reaction with hydrogen–carbon monoxide, *Int. J. Miner. Metall. Mater.*, 29(2022), No. 10, pp. 1882-1890. https://doi.org/10.1007/s12613-022-2512-6

IJMMM WeChat

QQ author group

INTERNATIONAL JOURNAL OF
Minerals, Metallurgy and Materials

Research Article https://doi.org/10.1007/s12613-024-3007-4

Study on the ion behavior of solid-phase reaction synthesis of iron chromite at 1473 K

Yan Wang[1)], *Peiyuan Ni*[2),✉], *Yuling Liu*[3)], *and Tengfei Deng*[1),✉]

1) State Key Laboratory of Silicate Materials for Architectures, Wuhan University of Technology, Wuhan 430070, China
2) Key Laboratory of Ecological Metallurgy of Multi-metal Intergrown Ores of Education Ministry, School of Metallurgy, Northeastern University, Shenyang 110819, China
3) State Key Laboratory of Powder Metallurgy, Central South University, Changsha 410083, China
(Received: 10 May 2024; revised: 10 September 2024; accepted: 11 September 2024)

Abstract: The enrichment of chromium in the magnetic iron chromite ($Fe(Cr_xFe_{1-x})_2O_4$) phase is crucial for the recovery and recycling of chromium in stainless-steel pickling sludge. The kinetics and reaction mechanism of the solid-phase reaction between Fe_3O_4 and Cr_2O_3 were investigated using the diffusion couple method at 1473 K. Not only the diffusion behavior of Fe^{2+} ions and Cr^{3+} ions was elucidated, but also the solid solution behavior of Fe^{3+} ions was discussed clearly. The microscopic morphology of the diffusion couple and the change in the concentrations of Fe and Cr cations across the diffusion layers were analyzed using scanning electron microscopy and energy dispersive spectroscopy. The self-diffusion coefficients of cations were calculated based on the concentration profiles of Fe and Cr, with the results indicating that the self-diffusion coefficient of the Fe ions was consistently higher than that of the Cr ions. Additionally, a mixture of Fe_3O_4 and Cr_2O_3 was annealed at 1373–1473 K for 1–5 h, and the kinetic parameters were calculated by studying the phase content of the product. The phase content of $Fe(Cr_xFe_{1-x})_2O_4$ in the product was determined by Rietveld refinement of X-ray diffraction data, revealing that an activation energy (E) of 177.20 $kJ \cdot mol^{-1}$ and a pre-exponential factor (B) of 610.78 min^{-1} of the solid-phase reaction that produced the $Fe(Cr_xFe_{1-x})_2O_4$ spinel.

Keywords: diffusion couple; solid-phase reaction; kinetics; iron chromite

1. Introduction

Stainless steel is widely used in architectural decoration, transportation, aerospace, energy generation, and environmental and structural engineering protection owing to its good corrosion resistance, mechanical characteristics, formability, and long service life [1–4]. However, an oxide layer is produced on the surface of stainless steel during hot rolling and annealing, which reduces its corrosion resistance and adversely affects its performance [5–6]. Therefore, to improve surface quality and enhance corrosion resistance, the oxide layer is usually cleaned by acid pickling [7–8]. This surface treatment method typically uses hydrochloric, hydrofluoric, and sulfuric acids for pickling the oxide layer. During the treatment process, the metals on the surface layer are dissolved in a pickling solution to produce a large amount of metal-containing wastewater [9–11], which is precipitated by calcium hydroxide to form sludge. Stainless-steel pickling sludge contains many metals such as Fe, Cr, and Ca, among which Cr(III) ions are easily oxidized into highly toxic Cr(VI) ions in the air, which causes severe environmental pollution problems [12–13]. Therefore, to effectively address the issue of environmental pollution caused by sludge storage, it is crucial to find a way to achieve the recovery and recycling of chromium in the sludge.

Several treatment methods have been proposed to recover and recycle chromium from sludge. Zhang *et al*. [14] introduced microbial-induced carbonate precipitation to immobilize chromium in stainless-steel pickling sludge, and the results showed that the bacteria-based biomineralization process has excellent detoxification work on stainless-steel pickling sludge. However, this method is more suitable for lower chromium leaching concentrations, and its application is relatively limited. The pyrometallurgical process can directly reduce valuable metals in sludge at high temperatures of 1573–1773 K by adding carbon to the sludge to form a Fe–Cr alloy [10,15]. However, carbon allocation leads to the production of CO_2 gas during the treatment process, and the main $CaSO_4$ and CaF_2 in the sludge consequently produces volatile harmful gases, such as SO_3, when the temperature is higher than 1473 K, which is contrary to green environmental protection. Therefore, the development of an efficient and environmentally friendly pollution-free treatment method is particularly important for the recovery of chromium from sludge.

Spinel-structured materials with the general formula

✉ Corresponding authors: Peiyuan Ni E-mail: nipeiyuan@smm.neu.edu.cn; Tengfei Deng E-mail: dengtf@whut.edu.cn

AB_2O_4 are ceramic compounds that have garnered significant attention. In this formula, A(II) and B(III) represent cations. Depending on the characteristics of the constituent ions in the composition formula, these oxide materials can exhibit a wide range of physical properties, including good corrosion resistance, catalytic activity, electrical conductivity, dielectric properties, and magnetism [16–20]. As a result, they find extensive applications in various industrial fields such as refractory materials, catalysts, magnetic materials, superhard materials, gas sensors, and high-pressure sensors [21–24]. Among these spinel-structured materials, $Fe(Cr_xFe_{1-x})_2O_4$ iron chromite is considered one of the most important spinel compounds due to its excellent electronic and magnetic properties, which has attracted significant attention from researchers. The sludge mainly contains FeO_n, Cr_2O_3, and calcium-containing compounds. On one hand, FeO_n and Cr_2O_3 can be accurately redissolved into the $Fe(Cr_xFe_{1-x})_2O_4$ spinel phase in a temperature range of no more than 1473 K. On the other hand, due to the excellent magnetic properties of $Fe(Cr_xFe_{1-x})_2O_4$ spinel, it can be effectively separated from sludge using magnetic separation method. Therefore, Cr can be efficiently recovered from sludge through the synthesis of the $Fe(Cr_xFe_{1-x})_2O_4$ spinel via a solid-phase reaction. However, due to the high Fe element content in sludge systems, Fe ions often exist in the form of a mixture of Fe^{2+} and Fe^{3+} ions. This leads to the formation of iron chromium spinel in the sludge system differing from the traditional AB_2O_4 spinel formation. In addition to the diffusion behavior of Fe^{2+} and Cr^{3+}, Fe^{3+} is also dissolved into the iron chromium spinel, but the kinetic mechanism of this process remains unclear. Furthermore, due to the unclear kinetic parameters of $Fe(Cr_xFe_{1-x})_2O_4$ synthesis through the solid reaction of FeO_n and Cr_2O_3 and the diffusion rates of Fe and Cr cations, the experimental parameters for synthesizing a single-phase $Fe(Cr_xFe_{1-x})_2O_4$ cannot be precisely determined. Therefore, a kinetic study of the solid-phase reaction of FeO_n and Cr_2O_3 to produce $Fe(Cr_xFe_{1-x})_2O_4$ is essential for the efficient recovery of chromium elements.

The reaction between solid phases is mainly achieved by diffusion, and numerous studies have been conducted on solid-phase diffusion behavior, among which the diffusion couple method is widely used in solid-phase reactions for diffusion between metals and oxides [25–30]. Chen *et al*. [31–32] investigated the kinetics and reaction mechanism of the solid-state reaction between Cr_2O_3 and calcium ferrite using the diffusion couple method. X-ray diffraction (XRD) is widely used to study the solid-phase reaction mechanism and calculate the solid-phase reaction kinetic parameters. Kril' ová *et al*. [33] studied the kinetics of the solid-phase reaction of magnesium aluminate (MA) spinel formation from mechanically activated mixtures of both Mg and Al oxides and hydroxides via high-temperature XRD at elevated temperatures. The degree of conversion of the MA spinel formation was determined using the Rietveld method, and the rate constants and activation energies of the crystalline $MgAl_2O_4$ formation for the selected mixtures were calculated by fitting the kinetic data.

In this study, the solid-phase diffusion reaction of the product layer during iron chromite sintering was investigated. Fe_3O_4 and Cr_2O_3 were used as the raw materials to form the diffusion couple, and their solid-phase diffusion reactions were studied at 1473 K in Ar at different heat-preservation times. The solid-phase diffusion reaction mechanism of $Fe(Cr_xFe_{1-x})_2O_4$ sintering was clarified through the distribution of Fe and Cr in the diffusion couple, which provided guidance for obtaining high-value iron chromite. Simultaneously, the reaction mechanism was further confirmed by XRD, and the kinetic parameters of the reaction were calculated using the XRD data of the solid-phase reaction at 1373–1473 K. The degree of conversion of the $Fe(Cr_xFe_{1-x})_2O_4$ spinel formation was determined using the Rietveld refinement method, and the experimental conditions for the synthesis of single-phase $Fe(Cr_xFe_{1-x})_2O_4$ spinel were deduced.

2. Experimental

2.1. Materials

Cr_2O_3 and Fe_3O_4 cylindrical blocks (99.95% purity, diameter 20 mm, and height 10 mm; Beijing Zhongke Yannuo New Material Technology Co., Ltd., Beijing, China) were used in the diffusion experiment. The raw material Cr_2O_3 (99.99% purity, Tianjin Guangfu Technology Development Co., Ltd., Tianjin, China) and Fe_3O_4 powders (99.00% purity, Shanghai Aladdin Biochemical Technology Co., Ltd., Shanghai, China) were used for the solid-phase reaction experiments.

2.2. Procedure

The experiment was divided into two parts: a diffusion couple experiment and a solid-phase reaction of $Fe(Cr_xFe_{1-x})_2O_4$ synthesized using Cr_2O_3 and Fe_3O_4 powder. The diffusion behaviors of Cr_2O_3 and Fe_3O_4 were studied using the diffusion coupling method, as shown in Fig. 1(a). First, the raw material was pretreated, and a raw material block with a diameter of 20 mm was polished with SiC sandpaper to obtain a flat contact surface. Subsequently, as indicated by the green arrow in Fig. 1(a), the diffusion couple was obtained by fitting Cr_2O_3 and Fe_3O_4 cylinders with flat contact surfaces firmly together. The Mo crucible equipped with a Fe_3O_4–Cr_2O_3 diffusion couple was placed in a vertical high-temperature tube furnace with Ar gas. A temperature-measuring thermocouple was used to monitor the temperature continuously to ensure the accuracy of the set temperature. Diffusion couple experiments were performed at 1473 K. After stabilizing at the target temperature, the samples were annealed for 1, 3, 6, 9, and 12 h. The Mo crucible containing the sample was then raised to the air inlet, and the air flow was increased to achieve gas cooling.

As indicated by the blue arrow in Fig. 1(b), the $Fe(Cr_xFe_{1-x})_2O_4$ samples were prepared using a solid-phase synthetic method. Cr_2O_3 and Fe_3O_4 powders were weighed at a molar ratio of 1:1, and the raw materials were poured into an agate mortar and ground for approximately 30 min to ensure an even raw material mixture. A cylinder with a diamet-

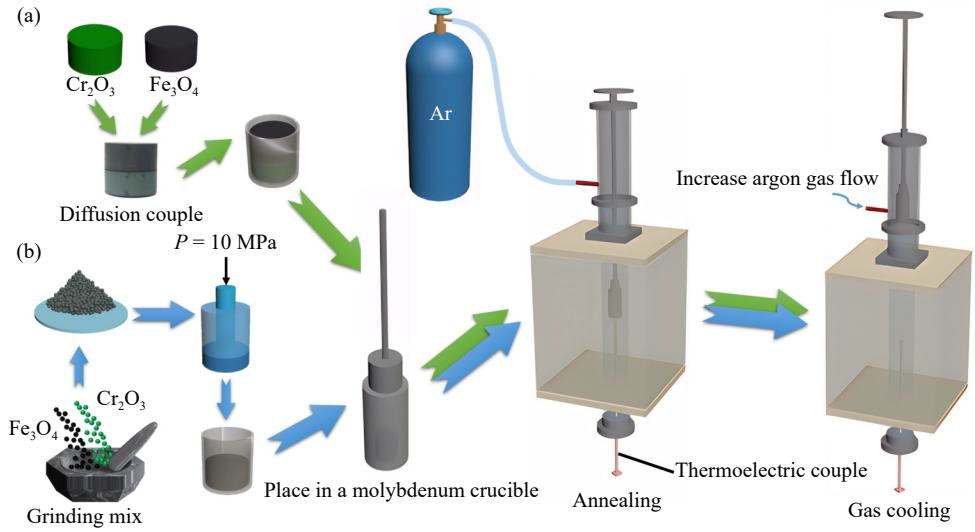

Fig. 1. Schematic of the (a) diffusion couple and (b) solid-phase reaction experiments.

er of 20 mm was obtained by holding a mixture of approximately 2 g in a tablet press at a pressure (P) of 10 MPa for 1 min. The cylinder was then placed in a Mo crucible, and the samples were then placed in a vertical high-temperature tubular Ar furnace. Solid-phase reaction experiments were performed at 1373, 1398, 1423, 1448, and 1473 K. After reaching the respective temperatures, the samples were annealed for 1, 2, 3, 4, and 5 h, respectively, and then gas-cooled by increasing the Ar flow rate.

2.3. Characterization

The sample obtained from the diffusion couple experiment was inlaid with acrylic resin and cut in the diffusion direction of the diffusion couple. The cutting surface was then polished with 240-, 400-, 800-, 1200-, and 1500-mesh SiC sandpaper to obtain a smooth diffusion interface. Microscopic observation and analysis of the elemental distribution in the samples were conducted using scanning electron microscopy (SEM; TESCAN CLARA) equipped with energy dispersive spectroscopy (EDS; Xplore 30). The solid-state synthesized materials were characterized using powder X-ray diffraction (XRD; D8 Advance) with a Cu K_α radiation source (wavelength λ = 1.540510 Å). The XRD data were collected in the 2θ range of 10°–80° at a scan rate of 3°·min^{-1}. The obtained XRD data were analyzed quantitatively by means of Rietveld refinement by implementing GSAS-Ⅱ software [34].

3. Results

3.1. Microscopic morphology of diffusion couple

Fig. 2 shows the cross-sectional SEM backscattered electron (BSE) images of the samples annealed at 1473 K and at varying durations (1–12 h). In the BSE image of a sample,

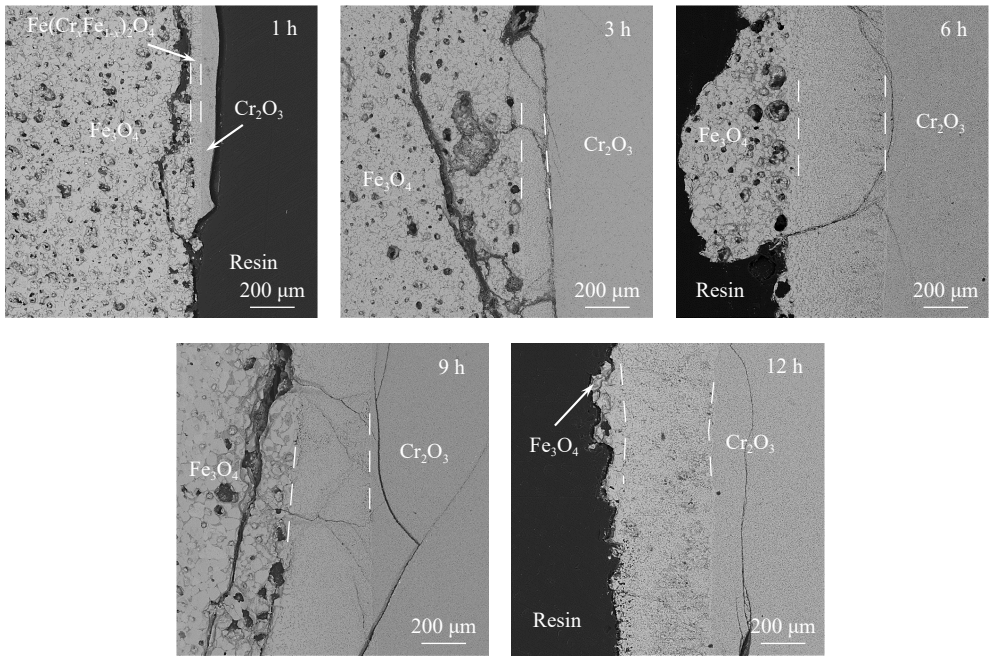

Fig. 2. SEM of the Fe_3O_4–Cr_2O_3 diffusion couples annealed at 1473 K and at varying durations (1–12 h).

the phases from left to right are Fe_3O_4, the product layer, and Cr_2O_3. The concentrated holes were more in the product layer near Fe_3O_4. The thickness of the product layer of the sample obtained at different annealing times was significantly different. As the annealing time increases, the thickness of the product layer progressively increases, then experiences a slight decrease before ultimately stabilizing. Multiple measurements of the product layer thickness of each sample were taken in the diffusion direction, and the measurement result is as shown in Fig. 3. The average thickness of the product layer at 1473 K with different annealing times is listed in Table 1. The average thickness of the product layer obtained by annealing for 1 h was 46.42 μm, which significantly increased to 138.60 μm when the annealing time was increased to 3 h. Furthermore, the thickness increased to 409.41 μm upon increasing the annealing time to 6 h. However, no significant difference was observed in the thickness of the product layer after annealing at 1473 K for 6, 9, and 12 h.

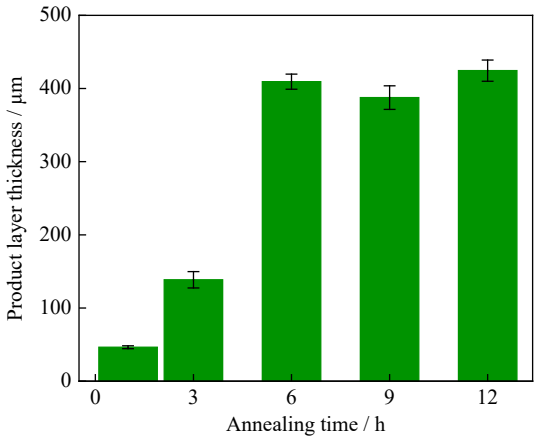

Fig. 3. Thickness of the product layer at 1473 K with different annealing times.

Table 1. The average thickness of the product layer at 1473 K with different annealing times

Annealing time / h	Product layer thickness / μm
1	46.42
3	138.60
6	409.41
9	387.55
12	424.42

Taking the Fe_3O_4–Cr_2O_3 diffusion couple annealed at 1473K for 9 h as an example (SEM–EDS analysis of Fe_3O_4–Cr_2O_3 diffusion couples annealed at different times at 1473K has been given in Fig. S1), the scanning analysis of the SEM–EDS diagram is depicted in Fig. 4(a). In the three regions with distinct boundaries, Cr, Fe, and O were distributed to different degrees. Fe was evenly distributed in the region of the Fe_3O_4 phase on the extreme left. Similarly, Cr was evenly distributed in the region of the Cr_2O_3 phase on the extreme right. The phase of the product layer was formed through the solid-state reaction between the diffusion couples and the mutual diffusion of Cr and Fe ions in the O-ion matrix. Fig. 4(b) shows the SEM–EDS line-scanning analysis of the Fe_3O_4–Cr_2O_3 diffusion couple at 1473 K for 9 h, with the line scan position marked by a yellow line in Fig. 4(a). Because the EDS of the oxygen content were inaccurate, the results were normalized to the elemental mole fraction with the oxygen content removed. The results of the line-scanning analysis showed that the elemental content in the product layer changed parabolically with distance, and the solid solubilities of Fe and Cr at different distances were different. That is, the contents of Fe and Cr in the $Fe(Cr_xFe_{1-x})_2O_4(0 \le x \le 1)$ phase were not fixed. In the middle product-layer region, the distribution density of Fe gradually decreased from left to right, whereas that of Cr increased. Due to Fe^{2+} and Fe^{3+} ions are difficult to distinguish using SEM–EDS, these ions were regarded as a whole and unified as Fe ions in this study. Assuming a constant mole fraction of Fe^{2+}, the cation content in the diffusion layer region is calculated based on the molar fraction of atoms within the dotted box in Fig. 4(b), as depicted in Fig. 4(c).

3.2. Calculation of ionic diffusion coefficient

Different models can be used to calculate the diffusion coefficients. In this study, the self-diffusion coefficients of different ions were calculated, and the diffusion coefficient D was subsequently calculated using Eq. (1).

$$C = \frac{M}{2(\pi Dt)^{\frac{1}{2}}}\exp\left(-\frac{d^2}{4Dt}\right) \tag{1}$$

$$M = 2A(\pi D)^{\frac{1}{2}} \tag{2}$$

where t and d are the diffusion time and distance, respectively; C is the diffusion ion concentration at time t and distance d; and M is the total amount of diffused material. M is represented by Eq. 2, where A is an integral constant. Based on Eqs. (1) and (2), logarithms can be taken on both sides. As shown in Eq. (3), ln$C$ has a linear relationship with d^2, and a is a constant.

$$\ln C = -\frac{d^2}{4Dt} + A = bd^2 + a \tag{3}$$

$$b = -\frac{1}{4Dt} \tag{4}$$

According to Eq. (3), b can be obtained by plotting d^2–ln C based on the concentration curves (Fig. 4(c)). Fig. 5 shows the linear fitting results of the Fe_3O_4–Cr_2O_3 diffusion couple at 1473 K for 1, 3, 6, 9, and 12 h; the b values and the fitted correlation coefficient r of $\widetilde{Fe}$, Fe^{3+} and Cr^{3+} ions at different diffusion times are also listed. The calculated self-diffusion coefficients of $\widetilde{Fe}$, Fe^{3+} and Cr^{3+} ions are presented in Table 2. Under different annealing times, the self-diffusion coefficient of ions consistently maintains the relationship of $D_{\widetilde{Fe}} > D_{Fe^{3+}} > D_{Cr^{3+}}$. When the annealing time was 1 h, the self-diffusion coefficients of $\widetilde{Fe}$, Fe^{3+} and Cr^{3+} ions were 0.35×10^{-8}, 0.22×10^{-8} and 0.63×10^{-9} $cm^2\cdot s^{-1}$, respectively. Upon increasing the annealing time, the self-diffusion coefficients of $\widetilde{Fe}$, Fe^{3+} and Cr^{3+} ions exhibited a slightly increas-

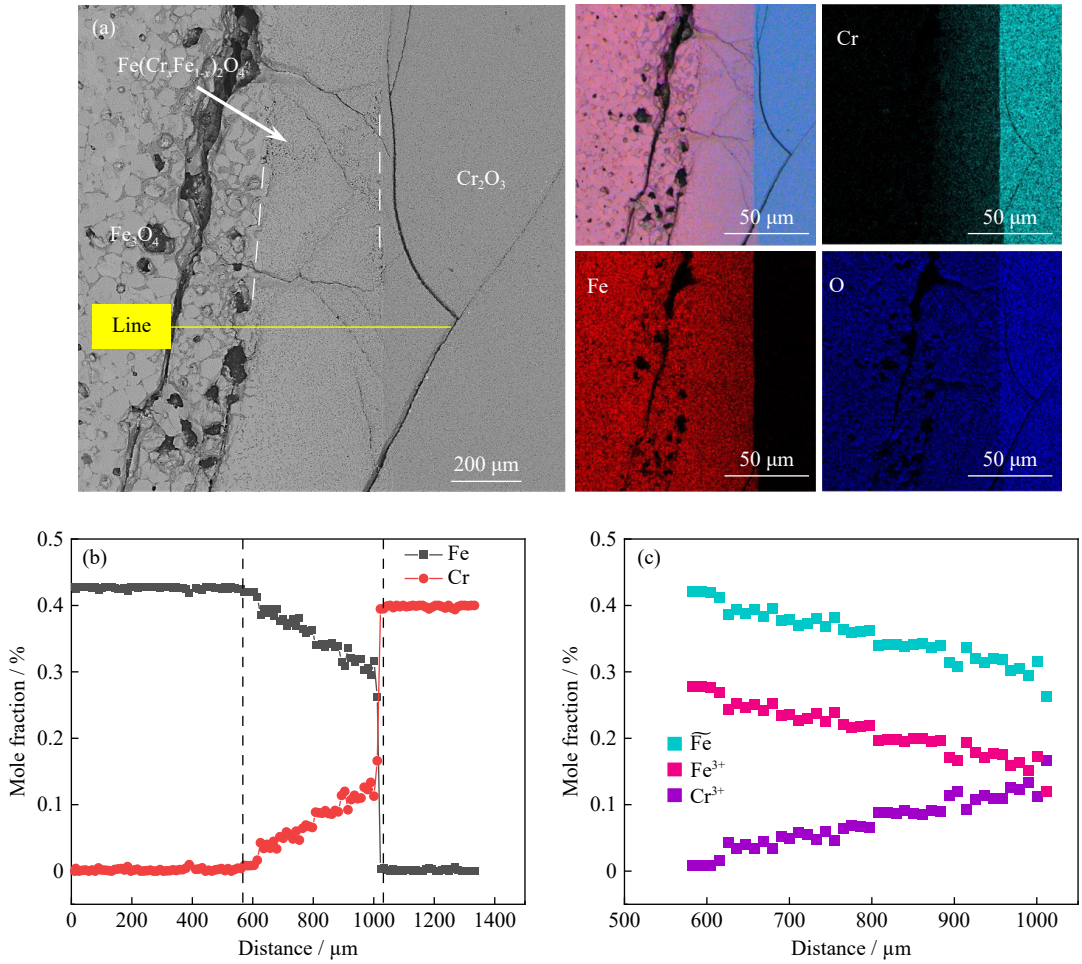

Fig. 4. (a) SEM–EDS map-scanning analysis, (b) SEM–EDS line-scanning analysis, and (c) concentration of cations at 1473 K for 9 h.

ing trend. When the annealing time was 6 h, the self-diffusion coefficients of $\widetilde{Fe}$, Fe^{3+} and Cr^{3+} ions were 7.41×10^{-8}, 4.37×10^{-8} and 1.13×10^{-8} $cm^2\cdot s^{-1}$, respectively. However, with a continuous increase of the annealing time, a tendency to stabilize after a slight decline was observed.

3.3. Characterization of solid-phase synthesized products

XRD analysis was performed on samples annealed at 1373–1473 K for 1–5 h, XRD patterns are given in Fig. S2. Fig. 6 shows the phase characterization of the samples obtained for 1373 and 1473 K at different annealing times. The XRD patterns were compared with the peak positions and strengths of the reference materials in the standard library, and the analysis revealed two phases: $FeCr_2O_4$ (PDF# 89-3855) and $Cr_{1.3}Fe_{0.7}O_3$ (PDF# 35-1112) in the sample. $FeCr_2O_4$ is a cubic crystal system with spinel structure, whereas $Cr_{1.3}Fe_{0.7}O_3$ is a rhombohedral crystal system with corundum structure. A series of $Fe(Cr_xFe_{1-x})_2O_4$ spinel with different x values have the same crystal structure, and exhibit the same diffraction characteristics on XRD patterns that cannot be distinguished. Therefore, the iron chromium spinel is collectively referred to as $Fe(Cr_xFe_{1-x})_2O_4$ phase. In particular, the solid-state reaction products of Fe_3O_4 and Cr_2O_3 are spinel $Fe(Cr_xFe_{1-x})_2O_4$ and sesquioxide $(Cr_{1-x}Fe_x)_2O_3$. The strongest peak positions for $Fe(Cr_xFe_{1-x})_2O_4$ and $(Cr_{1-x}Fe_x)_2O_3$ were 35.46° and 33.46°, respectively. By observing the diffraction intensity of these two peaks, the diffraction intensity of $Fe(Cr_xFe_{1-x})_2O_4$ was found to have increased gradually with increasing annealing time at the same temperature, while that of $(Cr_{1-x}Fe_x)_2O_3$ decreased gradually. At the same annealing time, the diffraction intensity of $Fe(Cr_xFe_{1-x})_2O_4$ was found to have increased gradually with increasing temperature, while that of $(Cr_{1-x}Fe_x)_2O_3$ decreased gradually. Thus, with an increase in the temperature and annealing time, the relative content of $Fe(Cr_xFe_{1-x})_2O_4$ gradually increased, whereas that of $(Cr_{1-x}Fe_x)_2O_3$ gradually decreased. Consequently, the sesquioxide generated by this reaction is unstable, and $(Cr_{1-x}Fe_x)_2O_3$ gradually transformed into $Fe(Cr_xFe_{1-x})_2O_4$ with increasing temperature and reaction time.

3.4. Quantitative analysis of the $Fe(Cr_xFe_{1-x})_2O_4$ spinel

XRD is the most effective technique for determining the phase contents of multiphase mixtures. Quantitative analysis of the $Fe(Cr_xFe_{1-x})_2O_4$ spinel was performed via Rietveld refinement of the XRD data. As shown in Fig. 6, the phases generated by the solid-phase reaction are crystalline, and the content of each phase in the mixture is obtained using the following formula:

$$W_a = \frac{m_a}{\sum m_i} = \frac{S_a Z_a N_a V_a}{\sum S_i Z_i M_i V_i} \quad (5)$$

where W_a, m, S, Z, N, and V are the content of phase a, phase

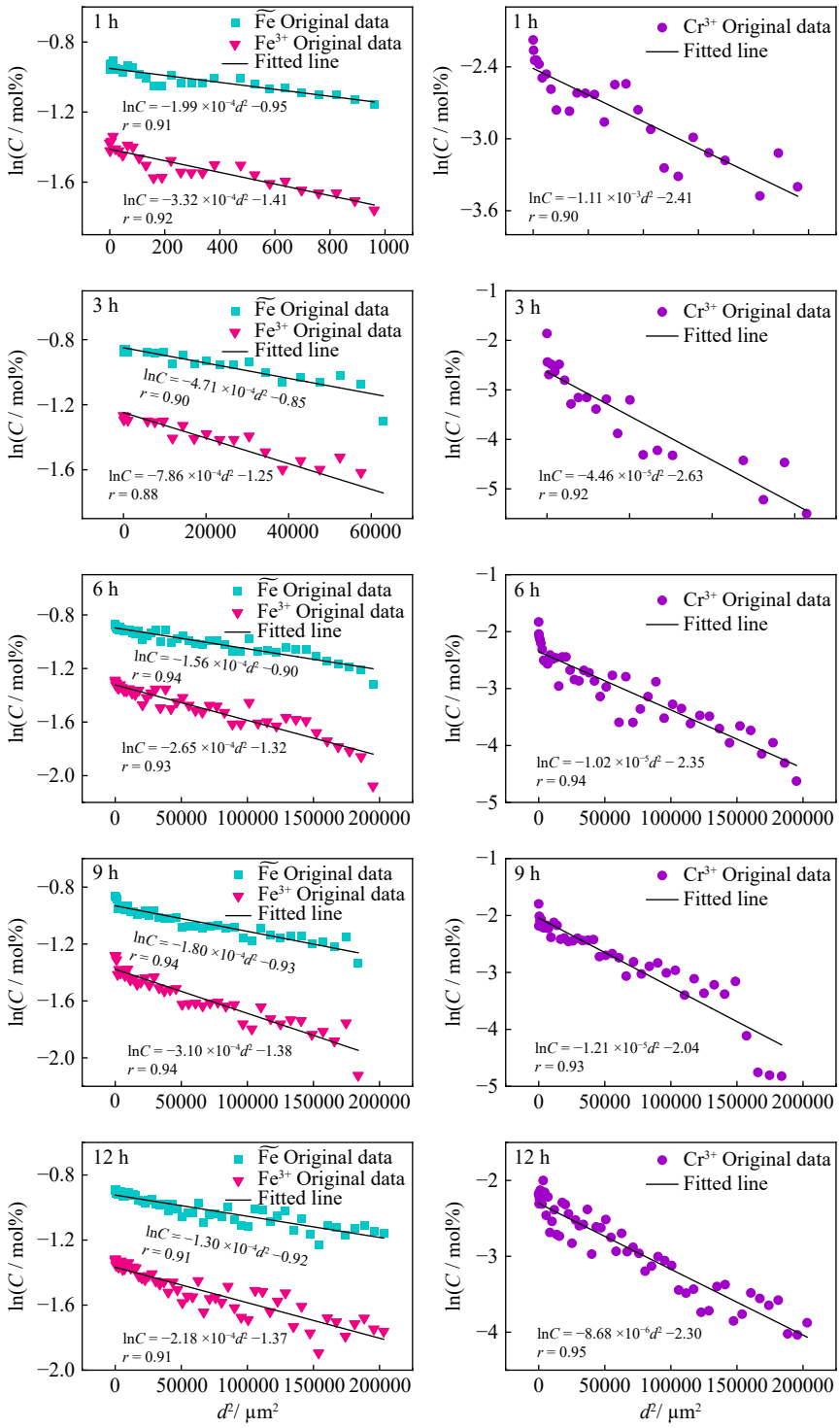

Fig. 5. Linear fitting results of the Fe_3O_4–Cr_2O_3 diffusion couple at 1473 K for 1–12 h.

Table 2. Self-diffusion coefficient of $\widetilde{Fe}$, Fe^{3+} and Cr^{3+} ions at different annealing times for 1473 K

Annealing time / h	$D_{\widetilde{Fe}}$ / (10^{-8} cm$^2\cdot$s^{-1})	$D_{Fe^{3+}}$ / (10^{-8} cm$^2\cdot$s^{-1})	$D_{Cr^{3+}}$ / (10^{-8} cm$^2\cdot$s^{-1})
1	0.35	0.22	0.063
3	4.92	2.94	0.519
6	7.41	4.37	1.130
9	4.30	2.49	0.636
12	4.44	2.65	0.667

mass, scale factor, number of formula units, and unit cell volume, respectively. Rietveld structure refinement can be used to obtain the scale factor S of each phase in the mixture such that the content of each phase can be determined.

Using the sample annealed at 1473 K for 5 h as a case study (the refined XRD pattern of samples annealed at 1373–1473 K for 1–5 h has been given in Fig. S3), the refined XRD pattern obtained through Rietveld analysis is illustrated in Fig. 7. In the graph, the black circles represent the original data points, and the pink line is obtained from the Ri-

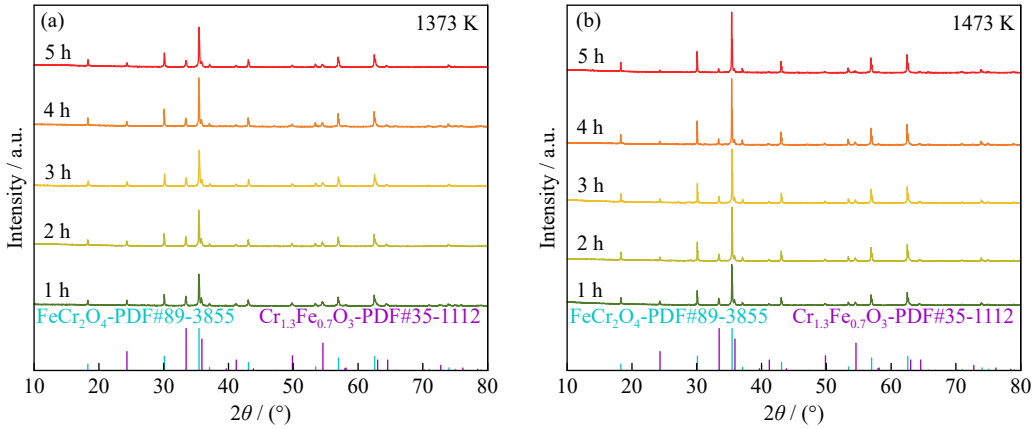

Fig. 6. Powder XRD patterns of samples obtained at different annealing times for (a) 1373 and (b) 1473 K.

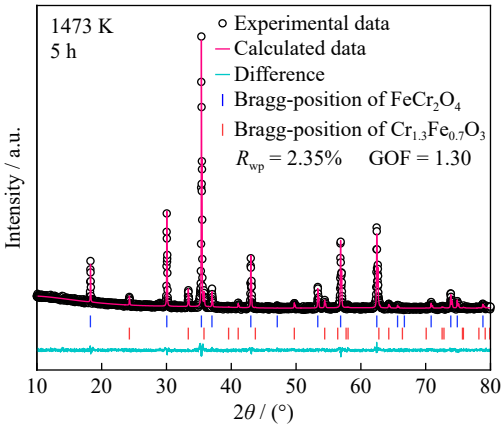

Fig. 7. Refined XRD patterns obtained via the Rietveld analysis.

Table 3. Phase content of $Fe(Cr_xFe_{1-x})_2O_4$ in the sample obtained by annealing at 1373–1473 K for 1–5 h

Temperature / K	Content / wt%				
	1 h	2 h	3 h	4 h	5 h
1373	59.63	62.36	64.77	67.70	69.80
1398	61.30	64.70	65.76	68.73	73.10
1423	65.50	66.95	71.60	74.40	77.17
1448	67.78	69.82	74.62	79.20	81.85
1473	70.30	76.39	78.28	82.80	88.34

etveld simulation. At the bottom of the graph, the aquamarine line represents the difference between the calculated XRD patterns and the experimental data, and the blue and red vertical lines represent the Bragg positions of phases $FeCr_2O_4$ and $Cr_{1.3}Fe_{0.7}O_3$, respectively. The weighted-profile *R*-factor (R_{wp}) and goodness of fit (GOF) for the XRD refinement of sample are illustrated in Fig. 7, which shows that refinement result satisfies $R_{wp} < 5\%$ and GOF < 2, indicating good quality and high reliability of the refinement performed. The phase content of $Fe(Cr_xFe_{1-x})_2O_4$ obtained via quantitative analysis is shown in Table 3, which indicates that the phase content of the spinel gradually increases with increasing annealing time at the same temperature. For the same annealing time, the phase content of the spinel gradually increases with increasing annealing temperature. The spinel content of the sample annealed at 1473 K for 5 h was 88.34wt%.

4. Discussion

4.1. Structural analysis

A more accurate crystal structure is obtained according to the Rietveld structure refinement described in Section 3.4. Fig. 8 shows the structural arrangement of the $Fe(Cr_xFe_{1-x})_2O_4$ spinel and $(Cr_{1-x}Fe_x)_2O_3$ sesquioxide obtained via structural refinement; Fe^{3+} and Fe^{2+} are represented by the red and orange spheres, respectively, whereas Cr^{3+} and O^{2-} are represented by the green and pink spheres, respectively. As shown in Fig. 8, in the unit cell structure of Fe_3O_4, the O^{2-} anions are the most tightly packed face-centered cubic, Fe^{2+} cations fill the tetrahedral void formed by O^{2-} ions, and Fe^{3+} cations occupy the octahedral void. In the unit cell structure of Cr_2O_3, O^{2-} anions are approximately hexagonal close packed (HCP) and Cr^{3+} cations fill the octahedral void formed by six O^{2-} ions. During the solid-phase reaction between Fe_3O_4 and Cr_2O_3, the Cr^{3+} ions replace the Fe^{3+} ions occupying the octahedral void in Fe_3O_4 to form the $Fe(Cr_xFe_{1-x})_2O_4$ spinel, and Fe^{3+} replaces part of the Cr^{3+} occupying the octahedral void in Cr_2O_3 to form the $(Cr_{1-x}Fe_x)_2O_3$ sesquioxide. However, as $(Cr_{1-x}Fe_x)_2O_3$ sesquioxide is not stable in this reaction, ultimately transforming into the $Fe(Cr_xFe_{1-x})_2O_4$ spinel phase.

4.2. Analysis of the reaction and diffusion mechanism

Fig. 9 shows the reaction of Fe_3O_4 and Cr_2O_3 to produce a spinel, which is composed of two processes: a chemical reaction at the phase interface and material migration in the solid-phase layer. Fig. 6(b) shows the solid-phase reactions of Fe_3O_4 and Cr_2O_3 at an ambient temperature of 1473 K. The reaction generated $Fe(Cr_xFe_{1-x})_2O_4$ and the byproduct $(Cr_{1-x}Fe_x)_2O_3$. Thus, the spinel formation process can be described as shown in Fig. 9. First, the reaction of Fe_3O_4 and Cr_2O_3 occurs to form $Fe(Cr_xFe_{1-x})_2O_4$ and $(Cr_{1-x}Fe_x)_2O_3$, as shown in Eq. (6). As the reaction time increases, the product layer gradually thickens, and $(Cr_{1-x}Fe_x)_2O_3$ is converted to $Fe(Cr_xFe_{1-x})_2O_4$, as shown in Eq. (7). The detailed mechanism of this process is further described in the following content.

$$Fe_3O_4 + Cr_2O_3 \rightarrow Fe(Cr_xFe_{1-x})_2O_4 + (Cr_{1-x}Fe_x)_2O_3 \quad (6)$$

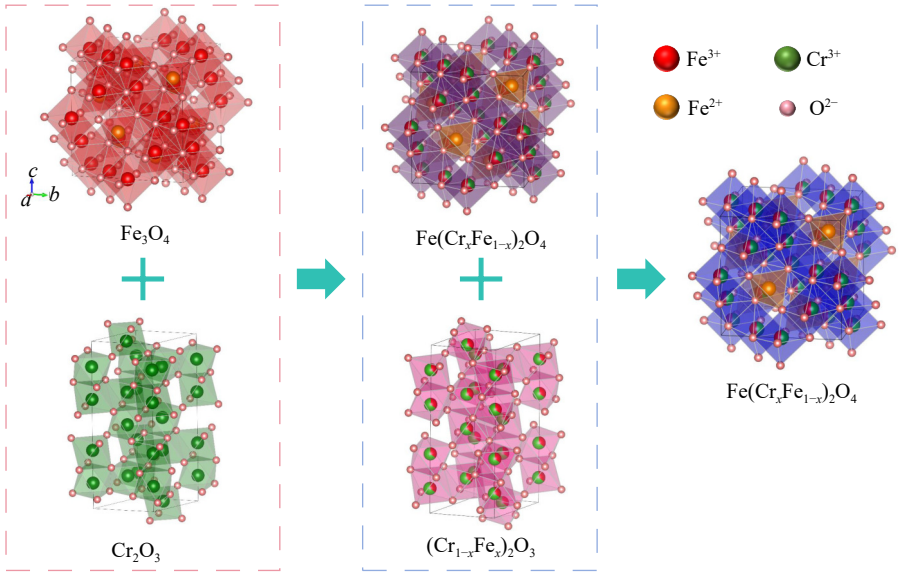

Fig. 8. Structural arrangement in the $Fe(Cr_xFe_{1-x})_2O_4$ spinel and $(Cr_{1-x}Fe_x)_2O_3$ sesquioxide.

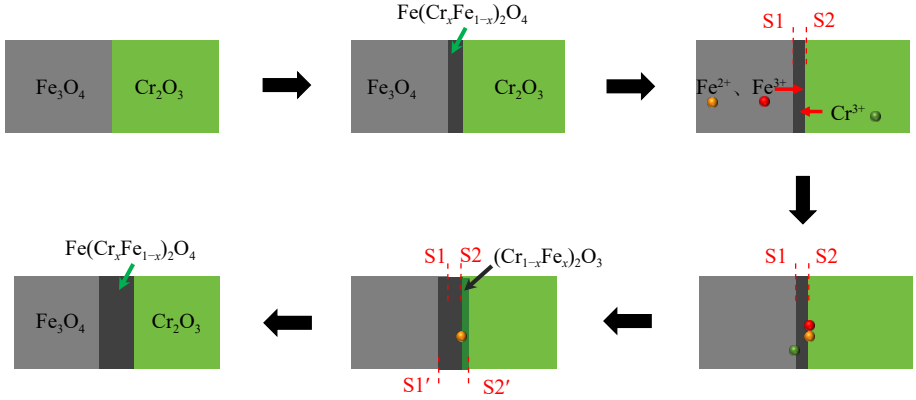

Fig. 9. Schematic of ion diffusion at the reaction interface of Fe_3O_4 and Cr_2O_3.

$$(Cr_{1-x}Fe_x)_2O_3 \rightarrow Fe(Cr_xFe_{1-x})_2O_4 \quad (7)$$

The reaction of Fe_3O_4 and Cr_2O_3 to produce the $FeCr_2O_4$ spinel is not a simple addition reaction but a superposition of displacement and transformation reactions. However, because the transformation reaction in Eq. (7) was performed in only one solid phase, the products of the entire reaction were treated as the same product layers to be studied. After the formation of the intermediate layer of the reaction product, the reverse diffusion of $\widetilde{Fe}$ and Cr ions through the product layer and the interface between the two oxides became the influencing factors for further spinel formation. Oxygen ions do not participate in the diffusion and migration processes. Eq. (8) shows the reaction at interface S1 in Fig. 9 because of the diffusion of Cr ions through the product layer; Cr ions are dissolved into Fe_3O_4 to form the $Fe(Cr_xFe_{1-x})_2O_4$ spinel. The reaction at interface S2 owing to the diffusion of $\widetilde{Fe}$ ions through the product layer is shown in Eq. (9), Fe^{3+} ions dissolve into Cr_2O_3 to form sesquioxide $(Cr_{1-x}Fe_x)_2O_3$; $(Cr_{1-x}Fe_x)_2O_3$ then combines with Fe^{2+} ions to form spinel $Fe(Cr_xFe_{1-x})_2O_4$ is shown in Eq. (10). Furthermore, it can be observed from Section 3.2 that $D_{\widetilde{Fe}} > D_{Fe^{3+}}$, indicating that Fe^{2+} and Fe^{3+} exhibit different diffusion rates during the diffusion process. Due to the higher octahedral crystal field stabilization energy of metal ions compared to tetrahedral crystal field stabilization energy, Fe^{2+} is more easily than Fe^{3+} separated from the crystal structure of Fe_3O_4. It is speculated that the diffusion rate of Fe^{2+} is much higher than that of Fe^{3+}, which also better confirms that the sesquioxide can rapidly bind Fe^{2+} and eventually transform into the spinel phase.

$$2xCr^{3+} + Fe_3O_4 = Fe(Cr_xFe_{1-x})_2O_4 + 2xFe^{3+} \quad (8)$$

$$2xFe^{3+} + Cr_2O_3 = (Cr_{1-x}Fe_x)_2O_3 + 2xCr^{3+} \quad (9)$$

$$3Fe^{2+} + 4(Cr_{1-x}Fe_x)_2O_3 = 3Fe(Cr_xFe_{1-x})_2O_4 + (14x-6)Fe^{3+} + (8-14x)Cr^{3+} \quad (10)$$

As the solid-phase reaction and diffusion progressed, interfaces S1 and S2 move to S1′ and S2′, respectively. Because the diffusion rates of the cations are not the same, the degree of migration of the diffusion interface also differs. Because the self-diffusion coefficient $D_{\widetilde{Fe}}$ of $\widetilde{Fe}$ ions in the diffusion system is greater than the D_{Cr} of Cr ions, the diffusion flux $J_{\widetilde{Fe}}$ is greater than J_{Cr}. In the diffusion process, the ion number of $\widetilde{Fe}$ through unit area per unit time is larger than that of Cr, and the degree of migration of diffusion interface S2 is greater than that of diffusion interface S1. This also explains the relatively concentrated holes on the side of the

product layer near the Fe_3O_4 phase, as shown in Fig. 2. The diffusion velocity of $\widetilde{Fe}$ ions is much higher than that of Cr ions during the diffusion process, resulting in unequal ion exchange. Moreover, the shrinkage of the crystal was not complete during the heat-preservation process, which led to relatively concentrated vacancies on the side of the ions with a faster diffusion rate. Holes were formed when the total number of vacancies on the side with faster-diffusion-rate ions exceeded the equilibrium vacancy concentration. These holes formed during the diffusion process are an important phenomenon of the Kirkendall effect, which provides the most direct evidence for the vacancy diffusion mechanism of solid diffusion [35–36].

As the reaction progressed, the product layer thickened. When the intermediate layer was initially formed, the spinel grains were not fully developed, the product layer was not dense, and the diffusion resistance of ions through the product layer was insignificant. As the reaction continued, the product layer gradually became denser, the spinel grains developed more fully, and the diffusion resistance of the ions through the product layer was much greater than the interfacial resistance. Meanwhile, the interfacial resistance of the phase was negligible, and the reaction speed was determined by the diffused ion current. This corroborated the diffusion coefficient at an annealing time of 9 h, which was slightly lower than that at an annealing time of 6 h. This is because the product layer becomes dense and ion diffusion is blocked, which slightly reduces the diffusion flux.

4.3. Analysis of product-layer thickness

When the resistance of the phase interface is sufficiently small to be ignored, a local thermodynamic equilibrium is reached at the phase interface, and the reaction rate measured by the experiment follows the parabolic law. As shown in Table 1, the product layer gradually thickened over time; however, after the annealing time was increased to 6 h, the thickness of the product layer remained stable. Once the product layer reaches a certain thickness, the resistance to ion diffusion through the product layer increases, causing a decrease in diffusion flux and a slower growth rate of the product layer. Consequently, the diffusion of the ion flow determines the reaction rate, and its diffusion flux is inversely proportional to the thickness of the product layer and directly proportional to the instantaneous growth rate of the product-layer thickness. Assuming that the diffusion activation energy of the system is constant, the diffusion coefficient of the system can be expressed by Eq. (11), where L is the thickness of the product layer and t is the annealing time. The diffusion coefficient $\widetilde{D}$ in Eq. (11) differs from the self-diffusion coefficients $D_{\widetilde{Fe}}$ and D_{Cr} of the ions studied previously and is the comprehensive diffusion coefficient of the system.

$$L^2 = 4\widetilde{D}t \tag{11}$$

As shown in Fig. 10, the thickness of the reaction product layer was proportional to the square root of time. Eq. (12) can be obtained by fitting the relationship between the change in product-layer thickness and the square root of the annealing time.

$$L = 2.11t^{1/2} \tag{12}$$

Further calculations yielded the comprehensive diffusion coefficient $\widetilde{D} = 1.11\times10^{-8}\,cm^2\cdot s^{-1}$ of the system at an annealing temperature of 1473 K. The comprehensive diffusion coefficient $\widetilde{D}$ does not represent the diffusion coefficient of an atom, that is $\widetilde{D} \neq D_{\widetilde{Fe}} \neq D_{Fe^{3+}} \neq D_{Cr^{3+}}$.

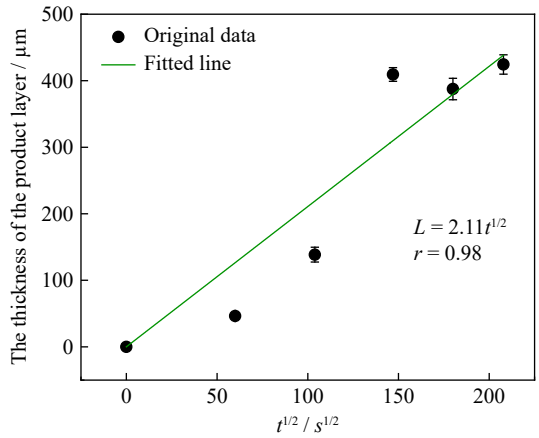

Fig. 10. Thickness of the product layer for different annealing times at 1473 K.

4.4. Calculation of kinetic parameters of reaction

The phase contents of $Fe(Cr_xFe_{1-x})_2O_4$ are listed in Table 3. The degree of conversion G of $Fe(Cr_xFe_{1-x})_2O_4$ can be defined as follow:

$$G = \frac{w_1}{w_1 + w_2}\times 100\% \tag{13}$$

where w_1 and w_2 are phase contents of $Fe(Cr_xFe_{1-x})_2O_4$ and $(Cr_{1-x}Fe_x)_2O_3$ respectively. Considering that the cross-sectional area of the reaction varies with the reaction process, the Ginstling–Brounshtein equation shown in Eq. (14) was used to calculate the reaction rate constant, where k is the reaction rate constant, and t is the annealing time.

$$F(G) = 1 - \frac{2}{3}G - (1-G)^{\frac{2}{3}} = kt \tag{14}$$

As shown in Fig. 11, t and $[1-2/3G-(1-G)^{2/3}]$ were plotted in the scatter plot. According to the scatter plot, $F(G)$ and t were found to be linear, which is consistent with the selected Ginstling–Brounshtein equation, further indicating diffusion to be the controlling step for the solid-phase reaction. In particular, the chemical reaction rate is much higher than the diffusion rate, the resistance of the reaction mainly originates from the diffusion rate, and the reaction is within the range of diffusion kinetics, which is consistent with the reaction and diffusion mechanisms described in Section 4.2. The linear fitting results of t–$F(G)$ are shown in Fig. 11, where the dark blue line is the fitting line obtained from the linear regression analysis, and its slope is the reaction rate constant k value. The value of k increased with increasing temperature. When the annealing temperature increased from 1373 to 1473 K, the reaction rate constant increased from 1.19×10^{-4} to

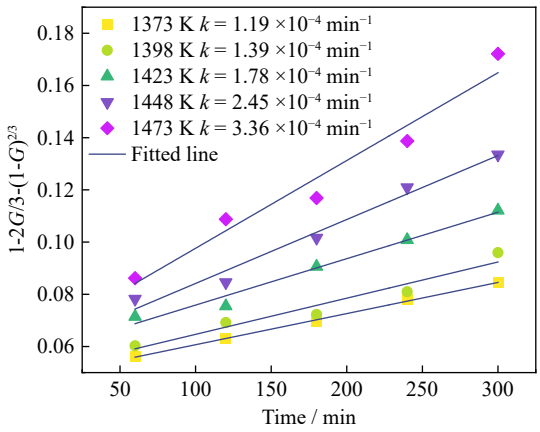

Fig. 11. Kinetic curve obtained from the treatment of the Ginstling–Brounshtein equation.

3.36×10^{-4} min^{-1}. The activation energy of the reaction was calculated using the Arrhenius equation shown in Eq. (15).

$$k = B\exp\left(-\frac{E}{RT}\right) \tag{15}$$

where B is the pre-exponential factor, E is the activation energy of reaction, T is the temperature, and R is the gas constant (R=8.31441 J·mol^{-1}·K^{-1}). Taking the logarithm of both sides of the equation to get Eq. (16), Fig. 12 was obtained by plotting $1/T$ and ln$k$, and the black line was obtained by linear fitting, whose equation is marked in the figure. From this, the values of activation energy (slope) and pre-exponential factor (intercept) were determined, and the kinetic parameters E =177.20 kJ·mol^{-1} and B = 610.78 min^{-1} were obtained by further calculation.

$$\ln k = -\frac{E}{R}\cdot\frac{1}{T} + \ln B \tag{16}$$

The empirical relationship between the reaction rate constant and the temperature can be obtained from the following kinetic parameters:

$$k = 610.78\exp(-2.13\times10^{4}/T) \tag{17}$$

From this, we calculated the reaction rate constant at each temperature using Eq. (17), and the time required for 100% spinel conversion was calculated using Eq. (14), according to the reaction rate constant. The annealing time required to obtain the single-phase $Fe(Cr_xFe_{1-x})_2O_4$ spinel at 1473 K was calculated to be 992 min.

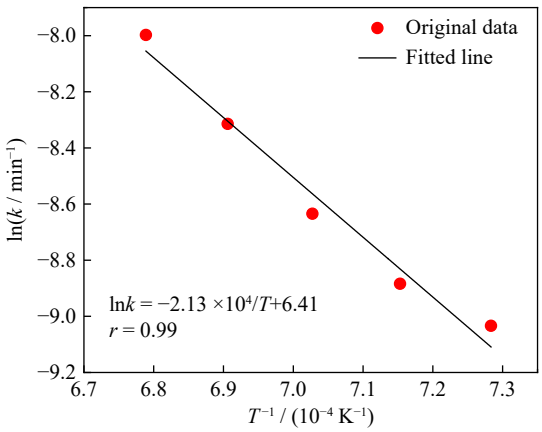

Fig. 12. Relation between the reaction rate constant and temperature.

5. Conclusions

A metallic oxide diffusion coupling method was applied to the interfacial reaction of Fe_3O_4–Cr_2O_3, wherein blocked Fe_3O_4 and Cr_2O_3 were incorporated into the diffusion couple to simulate the solid phase in the preheating layer during sintering. At an annealing temperature of 1473 K, the structure of the diffusion interface and the mechanism of the diffusion reaction are discussed by observing the microstructure of the diffusion layer and analyzing its components at different annealing times. Samples annealed for 1–5 h at 1373–1473 K were prepared by the solid-phase reaction method, and their XRD data were refined via Rietveld analysis for the crystal structure analyses and quantitative phase calculations. According to the quantitative analysis results of the $FeCr_2O_4$ spinel, the Ginstling–Brounshtein and Arrhenius equations were used to calculate the kinetic parameters of the reaction. The following results were obtained:

(1) At a temperature of 1473 K, the solid-phase reaction occurred in the Fe_3O_4–Cr_2O_3 diffusion couple and $Fe(Fe_{1-x}Cr_x)O_4$ was generated at the diffusion interface. The self-diffusion coefficients of Fe and Cr ions in the middle layer were calculated, which revealed that the $D_{\overline{Fe}} > D_{Fe^{3+}} > D_{Cr^{3+}}$ relationship existed invariably.

(2) With increasing annealing time, the product layer gradually thickened initially and then tended to stabilize. When the annealing time was 6 h, the product-layer thickness was 409.41 μm. Subsequently, the thickness remained almost unchanged, owing to the limited diffusion of cations in the product layer. The relationship between the product layer thickness and time at 1473 K was obtained.

(3) Diffusion of cations in the product layer was the driving force for the solid-phase reaction. As the reaction progressed and the product layer thickened, the diffusion of cations in the product layer became the control unit of the solid-phase reaction.

(4) The solid-phase reaction to generate $Fe(Cr_xFe_{1-x})_2O_4$ spinel was demonstrated in the crystal structure change by the substitution of Cr^{3+} ions for Fe^{3+} ions occupying the octahedral voids formed by O^{2-} ions in Fe_3O_4.

(5) The kinetic parameters for the synthesis of $Fe(Cr_xFe_{1-x})_2O_4$ by the solid-phase reaction were determined: the activation energy (E) was 177.20 kJ/·mol^{-1}, the pre-exponential factor (B) was 610.78 min^{-1}, and the annealing time required for obtaining the single-phase $Fe(Cr_xFe_{1-x})_2O_4$ spinel at 1473 K was 992 min.

Acknowledgements

This work was financially supported by the National Natural Science Foundation of China (No. 52274306) and Open Fund of State Key Laboratory of Silicate Materials for Architectures (Wuhan University of Technology), China (No. SYSJJ2020-03).

Conflict of Interest

All authors do not have competing interests to declare.

Supplementary Information

The online version contains supplementary material available at https://doi.org/10.1007/ s12613-024-3007-4.

References

[1] Y.H. Li, Y.D. Yang, Y.L. Huang, Z.T. Zhang, F. He, and H.L. Yang, A sustainable process for the resource utilization and stabilization disposal of stainless steel pickling sludge, *JOM*, 74(2022), No. 10, p. 3910.

[2] M. Rabi, K.A. Cashell, and R. Shamass, Flexural analysis and design of stainless steel reinforced concrete beams, *Eng. Struct.*, 198(2019), art. No. 109432.

[3] I. Vlčková, P. Jonšta, Z. Jonšta, P. Váňová, and T.Kulová, Corrosion fatigue of austenitic stainless steels for nuclear power engineering, *Metals*, 6(2016), No. 12, art. No. 319.

[4] J. Yuan and Z.N. Ou, Research progress and engineering applications of stainless steel-reinforced concrete structures, *Adv. Civ. Eng.*, 2021(2021), No. 1, art. No. 9228493.

[5] H.Y. Wang, Y. Li, S.Q. Jiao, and G.H. Zhang, Preparation of Ni–Fe–S matte and Fe–Cr–Si alloy by the co-treatments of stainless steel pickling sludge and electroplating sludge, *Metall. Mater. Trans. B*, 54(2023), No. 6, p. 3229.

[6] X.M. Li, G. Xie, M. Hojamberdiev, Y.R. Cui, and J.X. Zhao, Characterization and recycling of nickel- and chromium-contained pickling sludge generated in production of stainless steel, *J. Cent. South Univ.*, 21(2014), No. 8, p. 3241.

[7] C.H. Shi, Y.Q. Zhang, S. Zhou, J.C. Jiang, X.Y. Huang, and J. Hua, Status of research on the resource utilization of stainless steel pickling sludge in China: A review, *Environ. Sci. Pollut. Res. Int.*, 30(2023), No. 39, p. 90223.

[8] P.Y. Shi, H.N. Shi, C.J. Liu, and M.F. Jiang, Effect of pickling process on removal of oxide layer on the surface of ferritic stainless steel, *Can. Metall. Q.*, 57(2018), No. 2, p. 168.

[9] J.X. Zhao, Z.Y. Zhao, R.M. Shi, X.M. Li, and Y.R. Cui, Issues relevant to recycling of stainless-steel pickling sludge, *JOM*, 70(2018), No. 12, p. 2825.

[10] C.C. Yang, J. Pan, D.Q. Zhu, Z.Q. Guo, and X.M. Li, Pyrometallurgical recycling of stainless steel pickling sludge: A review, *J. Iron. Steel Res. Int.*, 26(2019), No. 6, p. 547.

[11] M.T. Wu, Y.L. Li, Q. Guo, D.W. Shao, M.M. He, and T. Qi, Harmless treatment and resource utilization of stainless steel pickling sludge *via* direct reduction and magnetic separation, *J. Cleaner Prod.*, 240(2019), art. No. 118187.

[12] F. Brück, A. Fritzsche, K.U. Totsche, and H. Weigand, Steel pickling rinse water sludge: Concealed formation of Cr(VI) driven by the enhanced oxidation of nitrite, *J. Environ. Chem. Eng.*, 5(2017), No. 3, p. 2163.

[13] C.L. Zhou, S.F. Ge, H. Yu, *et al.*, Environmental risk assessment of pyrometallurgical residues derived from electroplating and pickling sludges, *J. Cleaner Prod.*, 177(2018), p. 699.

[14] J.K. Zhang, P.D. Su, and L. Li, Bioremediation of stainless steel pickling sludge through microbially induced carbonate precipitation, *Chemosphere*, 298(2022), art. No. 134213.

[15] L.K. Singhal and N. Rai, Conversion of entire dusts and sludges generated during manufacture of stainless steels into value added products, *Trans. Indian Inst. Met.*, 69(2016), No. 7, p. 1319.

[16] A. Singh, R. Dawn, V.K. Verma, *et al.*, Electronic and magnetic properties of $FeCr_2O_4$ nanoparticles by advanced synchrotron based soft X-ray magnetic circular dichroism, *Physica B*, 647(2022), art. No. 414373.

[17] B. Chen, Y.J. Huang, J.N. Xu, *et al.*, Revealing the ductility of nanoceramic $MgAl_2O4$, *J. Mater. Res.*, 34(2019), No. 9, p. 1489.

[18] N.M.D. Vitorino, A.V. Kovalevsky, M.C. Ferro, J.C.C. Abrantes, and J.R. Frade, Design of $NiAl_2O_4$ cellular monoliths for catalytic applications, *Mater. Des.*, 117(2017), p. 332.

[19] H.F. Shang and D.G. Xia, Spinel $LiMn_2O_4$ integrated with coating and doping by Sn self-segregation, *Int. J. Miner. Metall. Mater.*, 29(2022), No. 5, p. 909.

[20] Y. Zhang, Z.H. Guo, Z.Y. Han, X.Y. Xiao, and C. Peng, Feasibility of aluminum recovery and $MgAl_2O_4$ spinel synthesis from secondary aluminum dross, *Int. J. Miner. Metall. Mater.*, 26(2019), No. 3, p. 309.

[21] L. Yang, Y.R. Zhang, C.P. Wu, *et al.*, A novel high-selectivity mixed potential ammonia gas sensor based on $FeCr_2O_4$ sensing electrode, *J. Electroanal. Chem.*, 924(2022), art. No. 116849.

[22] A. Ikesue and Y.L. Aung, Advanced spinel ceramics with highest VUV-vis transparency, *J. Eur. Ceram. Soc.*, 40(2020), No. 6, p. 2432.

[23] N. Lotfian, A. Nourbakhsh, S.N. Mirsattari, A. Saberi, and K.D. MacKenzie, A comparison of the effect of nanostructured $MgCr_2O_4$ and $FeCr_2O_4$ additions on the microstructure and mechanical properties of direct-bonded magnesia-chrome refractories, *Ceram. Int.*, 46(2020), No. 1, p. 747.

[24] F. Paborji, M. Shafiee Afarani, A.M. Arabi, and M. Ghahari, Solution combustion synthesis of $FeCr_2O_4$powders for pigment applications: Effect of fuel type, *Int. J. Appl. Ceram. Technol.*, 19(2022), No. 5, p. 2406.

[25] J. Chen, G.M. Xu, J.K. Xiao, and L.J. Zhang, Experimental investigations on the quinary interdiffusivities in diffusion couples of NiAlCoCr alloy/CoCrFeNi high-entropy alloys, *Calphad*, 76(2022), art. No. 102388.

[26] J.H. Dai, B. Jiang, J.Y. Zhang, *et al.*, Diffusion kinetics in Mg–Cu binary system, *J. Phase Equilib. Diffus.*, 36(2015), No. 6, p. 613.

[27] Y.F. Ouyang, K. Liu, C.Y. Peng, H.M. Chen, X.M. Tao, and Y. Du, Investigation of diffusion behavior and mechanical properties of Mg–Zn system, *Calphad*, 65(2019), p. 204.

[28] L. Gao, L. Zhou, C.S. Li, J.Q. Feng, and Y.F. Lu, Kinetics of stabilized cubic zirconia formation from MnO_2–ZrO_2 diffusion couple, *J. Mater. Sci.*, 48(2013), No. 2, p. 974.

[29] Z.S. Ren, X.J. Hu, X.X. Xue, and K. Chou, Solid state reaction studies in Fe_3O_4–TiO_2 system by diffusion couple method, *J. Alloys Compd.*, 580(2013), p. 182.

[30] W. Wei, H.R. Yue, and X.X. Xue, Diffusion coefficient of Ti^{4+} in calcium ferrite/calcium titanate diffusion couple, *Int. J. Miner. Metall. Mater.*, 27(2020), No. 9, p. 1216.

[31] B.J. Chen, T. Jiang, M. Zhou, L. Li, J. Wen, and Y.C. Wen, Interdiffusion kinetics and solid-state reaction mechanism between Cr_2O_3 and calcium ferrite based on diffusion couple method, *J. Alloys Compd.*, 865(2021), art. No. 158754.

[32] B.J. Chen, M. Zhou, T. Jiang, and L. Li, Observation of diffusion behavior between Cr_2O_3 and calcium ferrite based on diffusion couple method at 1373 K, *J. Alloys Compd.*, 802(2019), p. 103.

[33] L. Kril'ová and N. Števulová, The kinetic study of the synthesis of magnesium aluminate spinel from mechanochemically treated mixtures of oxide-hydroxide, *J. Mater. Sci.*, 39(2004), No. 16, p. 5403.

[34] B.H. Toby and R.B. Von Dreele, *GSAS-II*: The genesis of a modern open-source all purpose crystallography software package, *J. Appl. Crystallogr.*, 46(2013), No. 2, p. 544.

[35] F. Zhang, B.Y. Zhang, X.P. Chen, X.H. Zhang, X.K. Zhu, and H.S. Du, Computational simulation of voids formation and evolution in Kirkendall effect, *Physica A*, 554(2020), art. No. 124285.

[36] B. Wierzba, W. Skibiński, S. Wedrychowicz, and P. Wierzba, The voids kinetics during diffusion process, *Physica A*, 433(2015), p. 268.